Energy Band Alignment by Solution-Processed Aluminum Doping Strategy toward Record Efficiency in Pulsed Laser-Deposited Kesterite Thin-Film Solar Cell

Tong Wu, Juguang Hu, Shuo Chen, Zhuanghao Zheng, Michel Cathelinaud, Hongli Ma, Zhenghua Su, Ping Fan, Xianghua Zhang, Guangxing Liang

Energy Band Alignment by Solution-processed Aluminum Doping Strategy Towards Record Efficiency in Pulsed Laser-deposited Kesterite Thin-film Solar Cell

Tong Wu[1,2], Juguang Hu*[1], Shuo Chen[1], Zhuanghao Zheng[1], Michel Cathelinaud[1], Hongli Ma[2], Zhenghua Su[1], Ping Fan[1], Xianghua Zhang[2], Guangxing Liang*[1]

[1] *Shenzhen Key Laboratory of Advanced Thin Films and Applications, Key Laboratory of Optoelectronic Devices and Systems of Ministry of Education and Guangdong Province, College of Physics and Optoelectronic Engineering, Shenzhen University*

Shenzhen 518060, Guangdong, P. R. China

[2] *CNRS, ISCR (Institut des Sciences Chimiques de Rennes) UMR 6226, Univ Rennes*

Rennes, F-35000, France

*Corresponding author, E-mail: hujuguang@szu.edu.cn (Prof. Hu)

lgx@szu.edu.cn(Prof. Liang)

Keywords: Kesterite solar cell; Pulsed laser deposition; Energy band alignment; Carrier transport; Heterojunction heat treatment

Abstract

Kesterite-based Cu_2ZnSnS_4 (CZTS) thin-film photovoltaics involve a serious interfacial dilemma, leading to severe recombination of carriers and insufficient band alignment at CZTS/CdS heterojunction. Herein, an interface modification scheme by aluminum doping is introduced for CZTS/CdS via a spin coating method combined with heat treatment. The thermal annealing of the kesterite/CdS junction drives the migration of doped-Al from CdS to the absorber, achieving an effective ion substitution and interface passivation. This condition greatly reduces interface recombination and improves device fill factor and current density. The J_{SC} and FF of the champion device increased from 18.01 mA cm^{-2} to 22.33 mA cm^{-2} and 60.24% to 64.06% respectively, owing to the optimized band alignment and remarkably enhanced charge carrier generation, separation, and transport. Consequently, a photoelectric conversion efficiency (PCE) of 8.65% was achieved, representing the highest efficiency in CZTS thin-film solar cells fabricated by pulsed laser deposition (PLD) to date. This work proposed a facile strategy for interfacial engineering treatment, opening a valuable avenue to overcome the efficiency bottleneck of CZTS thin-film solar cells.

1. Introduction

Kesterite compound Cu_2ZnSnS_4 (CZTS) has attracted remarkable attention as an ideal absorber material for solar cells application, owing to its nontoxicity, natural abundance, cost-effectiveness, and high light absorption coefficient $\alpha > 10^4$ cm^{-1}. Nevertheless, the recorded photoelectric conversion efficiency (PCE) for CZTS and CZTSSe is $\approx$11.1%, and $\approx$13%, respectively,[1,2] which is still below the Shockley–Queasier (S–Q) limit ($\approx$31%), and considerably lower than its structural counterpart CIGS.[3-5] Many reasons may limit the efficiency of solar cells, particularly interfacial defects and unfavorable band alignment, which may bring about charge loss, nonradiative carrier recombination, and reduced minority carrier lifetimes. V_{OC} deficit and lower FF are the two dominant reasons for lower PCE.[6] As a known, traditional buffer layer, CdS shows unfavorable band-alignment with CZTS absorber. In addition, in CZTS, defects are generally formed near the interface because of their low formation energy. An efficient charge separation process at the PN heterojunction is very imperative for the effective operation of solar cells. The recombination at the PN heterojunction due to interface defects and poor band alignment is unfavorable for efficient solar cells. [7,8] The optimization of PN heterojunctions is the focal point of Kesterite CZTS research. The performance of solar cells can be improved via heterojunction engineering, cation doping, interfacial engineering, and passivation layer. [9-11] The Cd-free Al_2O_3 passivating layer and bandgap-controlled (Zn,Sn)O buffer layer enables CZTS and CZTSSe optoelectronic conversion gadgets with greater than 10% efficiency, displaying captivating industrial value. In particular, heterojunction engineering has achieved a breakthrough in the research of CZTS, for which, the efficiency of the device has been increased to 11%.[1] Similarly, the photoelectric performance such as V_{OC} and FF of CZTSSe-based devices, has been significantly improved

through high-temperature heat treatment. The problem of carrier recombination and interface defects at the heterojunction interface of CZTS has always been a major factor affecting the photoelectric conversion efficiency of cells. The built-in electric field and band bending are reduced with lower carrier concentration at the buffer layer/CZTS heterojunction. According to literature reports, alkali metal doping is usually used to lessen the band tails and bandgap while simultaneously increasing carrier concentration, thereby suppressing the interfacial and grain boundaries.[12-14] Some works enhance carrier concentration, and device performance by doping with trivalent In ions because the structure of kesterite (CZTS) is derived from the $CuInS_2$ of chalcopyrite structure. Al is usually used as an excellent dopant because of its similar properties and natural abundance compared with In. The concentration of dopant usually plays a crucial role in the doping effect. Impropriate concentration can even deteriorate the device's performance. Therefore, a controllable concentration of Al ion doping is achieved by annealing the multilayer structure ($AlCl_3$/CdS/CZTS) thereby minimizing the doping concentration of Al. Therefore, the N-type and P-type doping can be realized as ions penetrate through the buffer layer to the absorber layer. Fan et.al[15] achieved a device efficiency of 11.2% for a CZTS device prepared by a solution method through the heterojunction doping treatment of Al ions, thereby confirming that the doping of CZTS heterojunction can improve all aspects of the device performance.

In this work, regarding the quaternary CZTS compound, pulsed laser deposition (PLD) was selected to prepare CZTS thin film solar cells. PLD is an emerging technology for the preparation of thin film materials, which has advantages in the deposition of complex stoichiometric compounds while allowing good control of deposition rates. The laser pulses are performed on a typical microsecond time scale, and the ablative material transfers almost

stoichiometric from the target to the substrate.[16] After sulfuration, uniform and dense light absorbing layer CZTS thin film can be obtained. To further improve efficiency in CZTS thin-film solar cells, we developed an interface optimization method for doping heat treatment, where dopants were introduced during the two-step annealing process to achieve better optimization for CZTS/CdS heterojunction. That is, the CZTS/CdS heterojunction was first annealed by vacuum annealing in a tube furnace, followed by exposure to air on a hot stage. Prior to the second annealing, $AlCl_3$ was introduced on the surface of CdS by simple spin coating, thereby concurrently increasing the p and n-type carriers' concentrations at the CdS/CZTS heterojunction. The direct deposition on CZTS/CdS heterojunction of $AlCl_3$ for heat treatment promotes interdiffusion of Al, Cu, Cd, Zn, and Sn, between the two layers for efficient doping. On optimization, CZTS-based thin film solar cells deposited by PLD are improved to 8.65%, primarily due to high FF and J_{SC}. The short-circuit current density was increased to 23.22 mA cm^{-2}, and the FF is boosted to 64.05%. In addition, the effect of the doping heat treatment on the optical behaviors of thin films and photovoltaic properties of solar cells was investigated, suggesting a significant improvement in charge transportation. Further investigation exhibits that this condition may additionally be accredited to two key reasons: (i) two-step annealing passivates the interface defects and suppresses the charge recombination at the interface. (ii) Al^{3+} ion doping increases the carrier concentration and diminishes the cliff-type band-alignment at CdS/CZTS heterojunction. Furthermore, the overall enhancement in solar cell performance is related to the decrease in interfacial state density and the significant increase in minority carrier lifetime after doping heat treatment. The specific experimental scheme and characterization results were described in detail below in the following section.

2. Experimental section

CZTS sample preparation

Soda–lime glass (SLG) substrate was initially ultrasonically washed with deionized water, acetone, and ethyl alcohol. Then, a Mo layer was deposited by DC magnetron sputtering on SLG. The first layer thickness was 200 nm, and it deposited at 100 W DC sputtering power for 20 minutes. The second layer was almost 300 nm thick which were deposited at 250 W sputtering power for 30 minutes under 8×10^4 Pa. Precursors were then deposited with pulsed laser deposition method (PLD) under vacuum (5×10^4 Pa), as shown in **Figure 1(a)**. The KrF excimer laser (PLD-30, Shenzhen Shengfang Technology Co, Ltd, China) beam (248 nm wavelength, 7 ns pulse-width, and 10 Hz pulse repetition rate) was focused onto a sintered target with overall CZTS stoichiometry (5 cm diameter, and Cu:Zn:Sn:S = 24:15:12:49) at a spot size of 7 mm^2. Subsequently, the precursors were deposited for 50 minutes with laser energy of 150 mJ and substrate temperatures of 200 °C. For confirmation, with the composition uniformity of the 4×4 cm^2 precursor film, the scanning laser aimed at the CZTS target with 20 mm/s and the sample continuously rotated with 10 rounds/min. The precursor film was uniform visually, and the thickness of the as-deposited precursor film was approximately 1.3 μm, as detected by the cross-section SEM images in **Figure 2**. For post-sulfurization, 0.2 g of highly pure sulfur powder (99.999%) and the as-deposited CZTS thin films were separately placed (25 cm apart) in a double-chamber vacuum tubular furnace (60 mm diameter). Argon gas was introduced into the chamber after evacuating with mechanical pump prior to sulfurization. The precursor films were then sulfurized by maintaining the sulfur source zone at 220 °C and the sample zone at 600 °C, and then cooled at room temperature.

Interface doping and device fabrication

Initially, cadmium sulfide (CdS) film with 50 nm thickness was deposited by chemical bath deposition (CBD) method. In this method, SLG substrates were vertically inserted in the mix solution of ammonia (14.8 M, 22 mL), $CdSO_4$ (0.015M, 20 mL), and deionized water (140 mL), thiourea (0.75 M, 20 mL) at 80 °C for 9 minutes. Heat treatment process was conducted at 250 °C for 10 minutes in Ar atmosphere to introduce elemental Cd interdiffusion. An additional CZTS/CdS heterojunction heat treatment at 250 °C for 10 min in argon atmosphere was designed to induce elemental Cd inter-diffusion and optimize the band alignment. Moreover, for interface doping, a solution containing Al^{3+} (made by dissolving 0.1 M $AlCl_3 \cdot 6H_2O$ powders in 2-methoxy ethanol) was spin-coated on top of the CdS/CZTS and then heated at 280 °C for 5min on a hot plate in the air; the heating curve is shown in Figure S2. Afterward, ITO layer of 400 nm thick (R=18 Ω/sq) was deposited using RF magnetron sputtering machine under pressure of 0.4 Pa at 120 W and a flow rate of 30 sccm. Lastly, thermally evaporated Ag electrodes were deposited on the surface of ITO. Total devices active area was 0.15 cm^2, which was defined after scribing. For the best device, 100 nm MgF_2 antireflection layer was deposited by thermal evaporation method.

Materials and device characterization

The X-ray diffraction (XRD) results of the CZTS films were obtained on an X-ray diffractometer (Rigaku, Ultima IV). SEM images of the morphology and cross-sectional for CZTS films and devices were obtained by SEM (SUPRA 55) under 3 kV. The elemental depth profiling was once bought through mildly sputtering the shape of the CdS/CZTS with 1 keV Ar^+ ions over an etching vicinity of 2.5 mm. The TEM lamellas, with a thickness of approximately a hundred nm, had been made with the use of a focused ion beam (FIB) with a micro-sampling device (FEI, Scios DualBeam). A low beam current of 0.3 nA used to be used

for thicknesses beneath 1 mm. In the ultimate sharpening step, the surface of the lamella was once polished with a gallium ion beam of 50 pA to reap the goal thickness of approximately 100 nm. The cross-sectional TEM pics and elemental distribution for the CZTS devices had been measured with the use of an instrument ((FEI/Thermo Fisher, Titan3 Cubed Themis G2) geared up with an EDS system. Raman and the steady-state photoluminescence (PL) spectral were obtained from a Raman spectrometer (LABRAM-HR, 532 nm) and a PL spectrometer (Edinburgh Instruments FLS 900) excited by a picosecond-pulsed diode laser (EPL-640) of 638.2 nm wavelength. The J-V of CZTS devices were measured using a source meter (Keithley, 2400 Source Meter), and AM 1.5 simulated sunlight (Zolix, SS150) was calibrated with a standard Si reference cell. External quantum efficiency (EQE) was performed using an EQE system (Zolix, Solar Cell Scan 100) with calibrated Si and InGaAs photodiodes as references. The capacitance–voltage (C–V) and driven level capacity profile (DLCP) were measured using a parameter analyzer (Keithley, 4200A-SCS) with a cryogenic platform (JANIS), which was carried out using an impedance analyzer at a frequency of 50 kHz with a DC bias voltage sweeping from –1.0 to 0 V; it was conducted at an AC amplitude of 30 mV and frequency of 50 kHz under the dark at room temperature. DLCP measurement was performed with a frequency of 1 kHz at a DC bias from –0.25 V to 0 V and AC amplitude from 0.015 V to 0.14 V. The time-resolved photoluminescence (TRPL) characterization was once carried out on a machine with the use of time-correlated single photon counting (TCSPC) (PicoQuant, FluoTime 300), excited at the wavelength of 532 nm and energy of 50 mW. Ultraviolet photoelectron spectroscopy (UPS) spectra were carried out by a photoelectron spectrometer (XPS, Thermo Fisher Scientific, ESCALAB 250Xi) with He I (21.22 eV) excitation lines. The

electrochemical impedance spectroscopy (EIS) was measured on CHI600E Electrochemical Workstation at 0 bias potential in darkness.

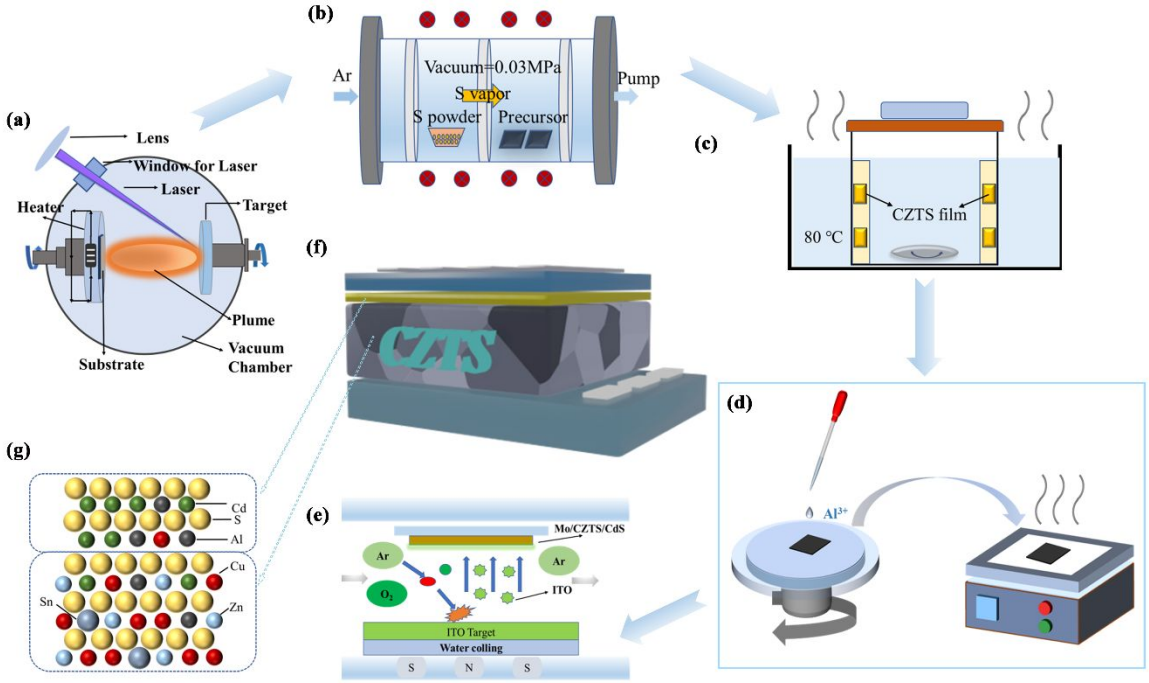

Figure 1. Schematic illustration of the device fabrication process: (a) Pulsed laser deposition for CZTS precursor, (b) Post-sulfurization of CZTS precursor, (c) Chemical bath deposition for CdS film, (d) Al^{3+} doping and heating treatment, (e) Sputtering ITO film. (f) CZTS solar cell structure; (g) CZTS/CdS molecular structure.

3. Result and discussion

We initially investigated the effect of different annealing methods on CZTS films prepared by PLD combined with post-sulfidation to determine the impact of annealing conditions on heterojunction doping. The XRD and Raman spectra of CZTS after vulcanization are shown in **Figure S1**. The peaks at 287 and 338 cm^{-1} are distinctive Raman peaks for CZTS, showing the higher phase purity and crystallinity prepared by PLD.[17] The key properties of CdS and CZTS film after annealing should be explored to fully understand the effect of the two-step thermal annealing process on the CZTS/CdS interface and solar cells' performance. **Figure S3** shows

the Raman and PL spectra of CZTS and CdS with different annealing methods, Raman analysis is directly irradiated on the deposited Glass/Mo/CZTS/CdS samples, and the laser is directly irradiated on the surface of cadmium sulfide to obtain the Raman information of CZTS and CdS at the same time, as shown in **Figure S3 (a)**. The peaks at 300 and 338 cm^{-1} denote the Raman shift of standard kesterite CZTS. Interestingly, the peak intensity of kesterite CZTS at 300 cm^{-1} should be weaker than 338 cm^{-1}. Moreover, the figure is contrary to that reported in the literature, probably due to the coincidence of the characteristic peaks of CZTS and surface CdS at 300 cm^{-1}. No other peaks appear in the figure except for a few obvious strong peaks, which indicates that the change in the annealing scheme of the heterojunction does not lead to the appearance of other phases in the absorption and buffer layers. The full-width analysis at the half-maximum range of each peak in the figure, indicates that the characteristic peaks of CdS are significantly sharper after heterojunction annealing, suggesting the significantly improved crystallinity of CdS by annealing treatment. In addition, steady-state photoluminescence (PL) was used to investigate the effect of different annealing schemes on the absorption layer (CZTS). Almost no change is found in the no-annealing sample (SS1) and the sample annealing in vacuum (SS2) in **Figure S3**, but the main peaks of the annealing of the samples in the air (SS3) and two-step annealing (SS4) have an evident red shift close to 50 nm, indicating more band tail states in the CZTS film. This condition may be caused by high-temperature thermal annealing in air, though its impact on device performance is negligible.[18-20] The main peaks of SS3 and SS4 were stronger and sharper, suggesting that the nonradiative recombination in the CZTS film was suppressed by annealing. During annealing in the open air, oxygen atoms may be entrenched into the grain boundaries of the CZTS films, leading to lower nonradiative charge recombination. Statistical distribution of device parameters (V_{OC}, J_{SC}, FF, and PCE) fabricated

by different annealing conditions are illustrated in **Figure S4** to obtain deep insight into heterojunction annealing on the photovoltaic performance of solar cells. The figure shows that the photoelectric conversion efficiency of the device obtained under various annealing parameters is higher than that of the untreated device, thereby revealing that heterojunction an important role in improving the PCE of the solar cells. Among them, V_{OC} and J_{SC} of the device annealed in a vacuum were remarkable improved, but the efficiency improvement was not obvious due to the significant decrease in the fill factor. By contrast, the two devices annealed in the air were significantly improved in all aspects, especially J_{SC} and FF. The J_{SC} of the device annealed in the air was increased to 21.46 mA cm^{-2} from the untreated 16.22 mA cm^{-2}, and the J_{SC} of the two-step annealed device was further increased to 21.8 mA cm^{-2}. In addition, a more uniform current distribution was obtained. A two-step annealing was introduced to boost the performance of CZTS; thus, the PCE reached 7.6%. In summary, Cd ions are thermally diffused to the absorption layer due to vacuum annealing, and the Cu_{Zn} defect density on the surface of the absorber layer is reduced. After annealing in air, oxygen atoms enter the heterojunction interface, effectively passivating the interface defects and suppressing the recombination of the carrier interface. As a result, J_{SC} and the FF have been significantly improved, thereby increasing the device efficiency. The champion devices obtained with different annealing approaches show a gradient change in the photocurrent–voltage characteristics (*J-V*) curve shown in **Figure S5 (a)** and EQE spectrum in **Figure S5 (b)**. The EQE spectra of all devices exhibit similar broad spectral responses from the ultraviolet to the near-infrared region, consistent with the properties of the CZTS. In addition, the maximum EQE response of the device fabricated by the two-step annealing process exceeds 80%, indicating the reduced carrier recombination at the CZTS/CdS interface and the passivated absorber layer. The short-circuit

current densities of each device obtained by integrating the spectral curves of EQE are 14.56, 16.03, 18.57, and 18.95 mA cm^{-2}, respectively, similar to the results obtained by the *J-V* test. The calculated band gap obtained from the EQE spectrum in the long wavelength range is shown in **Figure S5 (c)**. The figure shows that the band gap of the SS1 is closed to 1.62 eV and has not changed significantly. The band gap of SS3 and SS4 is reduced to 1.52 eV, which is close to the optimal band gap of CZTS thin film solar cells. Two-step annealing has significant gains in heterojunction quality and device performance. Therefore, we introduced ion doping prior to the second annealing to further modify the heterojunction interface. **Figure S3(c)** shows the Raman signal measured on the surface of CZTS/CdS heterojunction. All the strong peaks in the figure belong to the characteristic shift peaks of CZTS and CdS. The overlapping of peak shifts leads to a peak intensity at 298 cm^{-1} stronger than that at 333 cm^{-1} given that the characteristic peak positions of CZTS and CdS near 300 cm^{-1} are relatively close. No other characteristic peaks are shown in the figure, indicating the excellent crystallinity of CZTS and CdS, with little contribution to the generation of secondary phases caused by ion doping. For the Raman analysis of the Al-doped samples, we found that the main peak of CZTS has some redshift, which may be the result of doped Al entering the absorber layer. For CdS, there is also redshift at 592 cm^{-1} is also found, and the evidently sharper Al-doped Raman single at 592 cm^{-1} reflects the improvement in the CdS buffer layer.[21,22]

Figure 1 shows the preparation process of glass/Mo/CZTS/CdS/ITO/Ag/MgF_2 structure of thin film solar cells. We doped the heterojunction through spin coating shown in the figure after preparing the buffer layer by CBD method. **Figure 2(a)** shows the scanning electron microscopy (SEM) cross-section of CZTS thin film solar cell device. We obtained the absorption with large and penetrating grains, attributed to the preparation process of PLD

combined with sulfuring annealing. On this basis, the performance of thin-film solar cells is further optimized by heterojunction doping. For comparison, the best device performance of CZTS devices with different Al-doping levels is displayed in **Figure 2(b)**. The results of *J-V* and device parameters summarized in **Table 1**, show that under standard sunlight, the V_{OC} of the device increases from 589 mV undoped to 620 mV after doping, the FF increases from 60.24% to 64.03%, and the J_{SC} increased from 21.8 mA cm^{-2} to 23.56 mA cm^{-2}. After doping annealing, the photoelectric conversion efficiency increased by nearly 1% which reached 8.65%. **Table 2** shows the main parameters of CZTS prepared by PLD in recent years,[16, 23-27] and the development process of photoelectric conversion efficiency is shown in **Figure 2(c)**. This work exceeds the maximum PCE of CZTS solar cells prepared by PLD, indicating that PLD has great potential for optoelectronic devices.

Table 1. Device performance of CZTS solar cells with different doping concentration.

Sample	V_{oc} (mV)	J_{sc} (mA cm^{-2})	FF (%)	EFF (%)
A00	589	21.8	60.24	7.62
A10	595	22.66	63.45	8.35
A20	605	22.33	64.06	8.65
A30	592	21.98	55.21	7.03

Figure 2(d) shows the EQE spectra of Al-doped devices with different concentrations. The EQE spectra of all devices show similar broad spectral responses from the ultraviolet to the near-infrared region, consistent with the characteristics of the CZTS absorber layer. In addition, the maximum EQE response of all doped and undoped devices exceeds 80%, indicating lower recombination at the CZTS/CdS interface.[28] This result also corresponds to FF exceeding 60% for almost all our devices in this section. The short-circuit current densities of each device

obtained by the spectral curve integration of EQE are 19.06, 19.34, 19.90, and 17.68 mA cm^{-2}, consistent with J_{SC} obtained by the *J-V* test in the experiment. The integrated current density becomes slightly lower than the current density during the actual *J-V* test due to the optical loss during the test. The illustration in **Figure 2(e)** is the band gap calculated from the EQE spectrum in the long wavelength range. Evidently, the photoactive layer of the Al-doped device reduces the band gap from 1.52eV to 1.50eV, and the optical band gap of the buffer CdS from 2.42 eV to 2.40eV. The Urbach energy is usually used as a parameter to evaluate the band-tail state, which was calculated by ln(-ln(1-EQE)), and the reciprocal of its slope is derived when E-Eg is the x-axis.[29,30] As illustrated in **Figure 2(e)**, the E_U of CZTS devices with different doping concentrations is almost the same. The existence of the band tail state is usually caused by the fluctuation of the electrostatic potential, and the factor defining the extent of the electrostatic potential variation is caused by the defects in the CZTS absorber layer. As shown in the figure, the E_U of CZTS device decreased from 47.80 meV to 39.58 meV; a smaller EU value indicates an improvement of the disorder within the absorber layer material. The introduction of the band-tailed state not only affects carrier transport but also accelerates the recombination of photogenerated carriers. **Figure 2(f)** shows the PL spectra of different samples. The PL peak intensity of the Al-doped samples is significantly sharper, due to the reduction of nonradiative recombination in the CZTS absorber layer. It has an important contribution to the improvement of *V*oc and short-circuits current. The Eg (PL) after Al-doping as compared with pristine could be due to the increased Al content in kesterite given that the direct correlation of cation to Eg has already been identified.[31] In addition, the reduced $\Delta E_g = E_g(EQE) - E_g(PL)$ from≈110 meV (pristine) to ≈50 meV (Al-doped) indicates a suppressed band tailing behavior, which may be due to the reduced Cu-Zn antistite defects in the CZTS absorption layer. [13, 32,33]

Table 2. Comparison of key parameters in CZTS thin-film solar cells prepared by PLD.

	*V*oc (mV)	*J*sc (mV/cm^2)	FF (%)	EFF (%)		Ref
CZTS (N_2)	546	6.78	48.4	1.74	2007	[22]
CZTS (H_2S)	336	6.53	46.0	0.64	2008	[23]
CZTS (N_2+H_2S)	700	10.01	59.0	4.13	2012	[24]
CZTS (Ultra-thin)	616	17.6	47.9	5.2	2017	[25]
CZTS (Oxide route)	673	15.2	53.0	5.4	2020	[26]
CZTS (Sulfur)	642	18.40	56.21	6.62	2021	[27]
CZTS (Interfacial doping)	605	22.33	64.06	8.65	2022	This work

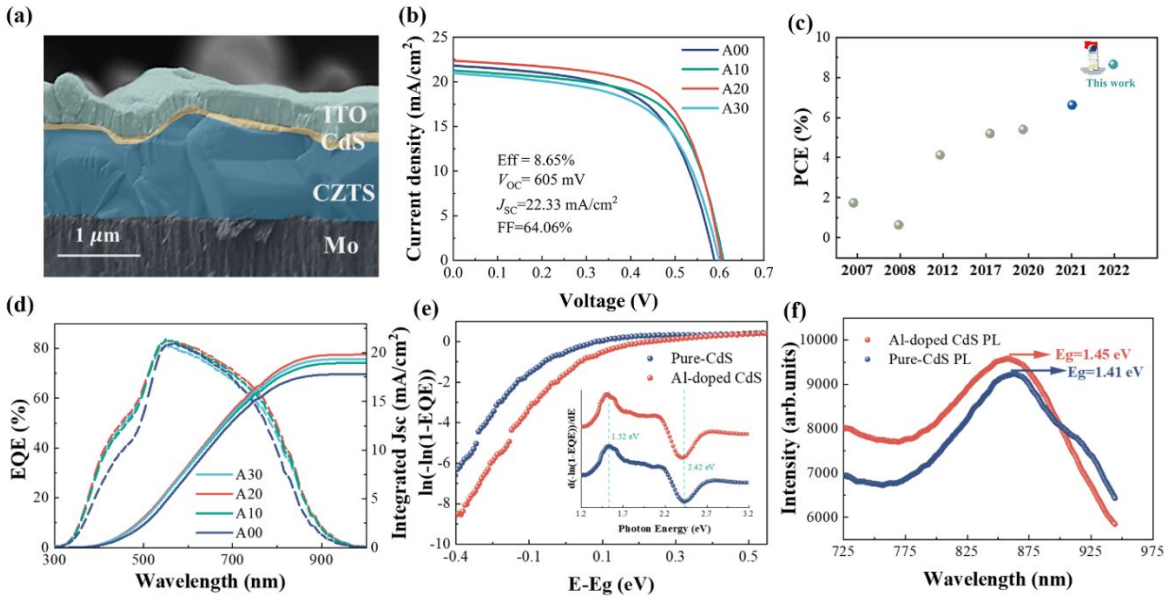

Figure 2. (a) Cross-sectional SEM image of the champion device. (b) *J-V* curve of CZTS solar cells with different doping concentration. (c) The development process of PCE for CZTS thin film solar cells prepared by PLD. (d) EQE spectra and the integrated J_{SC} of the devices with different doping concentration. (e) Urbach tail analysis for the pure-CdS and Al-doped CdS devices, inset shows the calculated band gap of CZTS and CdS. (f) The PL

spectrum of pure-CdS and Al-doped CdS devices.

Further tests have been conducted to illustrate the physical mechanism of the Al-doped device. Another key factor affecting device performance is the band alignment at CZTS/CdS, particularly conduction band offset (CBO) of the heterojunction. The mass-junction interface recombination has the characteristics of an important contribution, but most logarithmic conduction band offsets reported in the literature are characterized by a cliff-like (~ ─ 0.3 eV).[34-37] UPS measurements were performed on the surfaces of the dopant and undoped samples to explore the effect of Al ion doping on the energy band alignment at CZTS/CdS heterojunction interface. After Al ion doping treatment in the CdS layer, the band gap was obtained at 2.4 eV (as shown from the calculation and fitting of the band gap in EQE), and the work function decreased from 4.08 eV to 3.84 eV, representing the valence band maximum position (VBM), and the relationship with the Fermi level increased from 1.55 eV to 1.63 eV. In addition, the band-gap of CZTS was maintained at 1.50 eV, and its work function is increased from 4.22 eV to 4.32 eV after doping, indicating the reduction of secondary electron escape work after Al doping. This condition is beneficial for the enhancement of charge collection efficiency and may increase the current density. In the meantime, VBM of the absorption layer CZTS is reduced from 0.34 eV to 0.30 eV. These findings revealed that Al doping could concurrently enhance carrier concentrations of both (p-type and n-type) carriers (Figure 3).[11, 38]

Based on the aforementioned findings, the graph of the band structures of the two materials (CZTS and CdS) with and without Al-doping and their band alignment are shown in **Figures 3(e)** and **(f)**, respectively. The results show that the CBO values changed from negative to positive, suggesting a cliff-like band alignment between CZTS and CdS that turned out to be a spike-like band alignment. Moreover, the CBO value of the doped heterojunction increased

from -0.17 eV to 0.05 eV, indicating a relatively lower electron barrier at the interface and fewer electrons stationed at the interface.[39] Thus, the interface charge recombination loss is reduced. Meanwhile, the spike-like band alignment is beneficial to devise performance, especially for FF, consistent with the results of the previous *JV* test.

We performed conductive AFM (c-AFM) tests on the differently treated samples under illumination to detect the local current changes on the sample surface to further understand the doping effect on the photoelectron behavior of the heterojunction surface. Different from the non-contact measurement of KPFM, c-AFM records current fluctuations through a tip that contacts the sample surface to form a path with the sample surface. The position of the onset potential on the surface of the sample (the position where the onset potential increases sharply) was systematically analyzed by applying a relatively small bias voltage (1 V). As shown in the figure, the surface current profiles and topographic profiles have very similar correspondences, which are caused by the difference in the carrier concentration at the grain boundaries and on the grains. The current and surface topography distribution curves in **Figures 4(e)** and **(f)** are obtained from the current distribution diagrams in **Figures 4(c)** and **(d)**. The grain analysis shows that the current at the grain boundary has a significant weakening compared with other places, probably caused by the larger resistance at the grain boundary. In addition, the current on the surface of the sample after doping is increased by an order of magnitude, suggesting the higher carrier collection efficiency at the Al-doped sample surface. The microcurrents on the grain surface are also higher, remarkably improving the J_{SC} in solar cells.

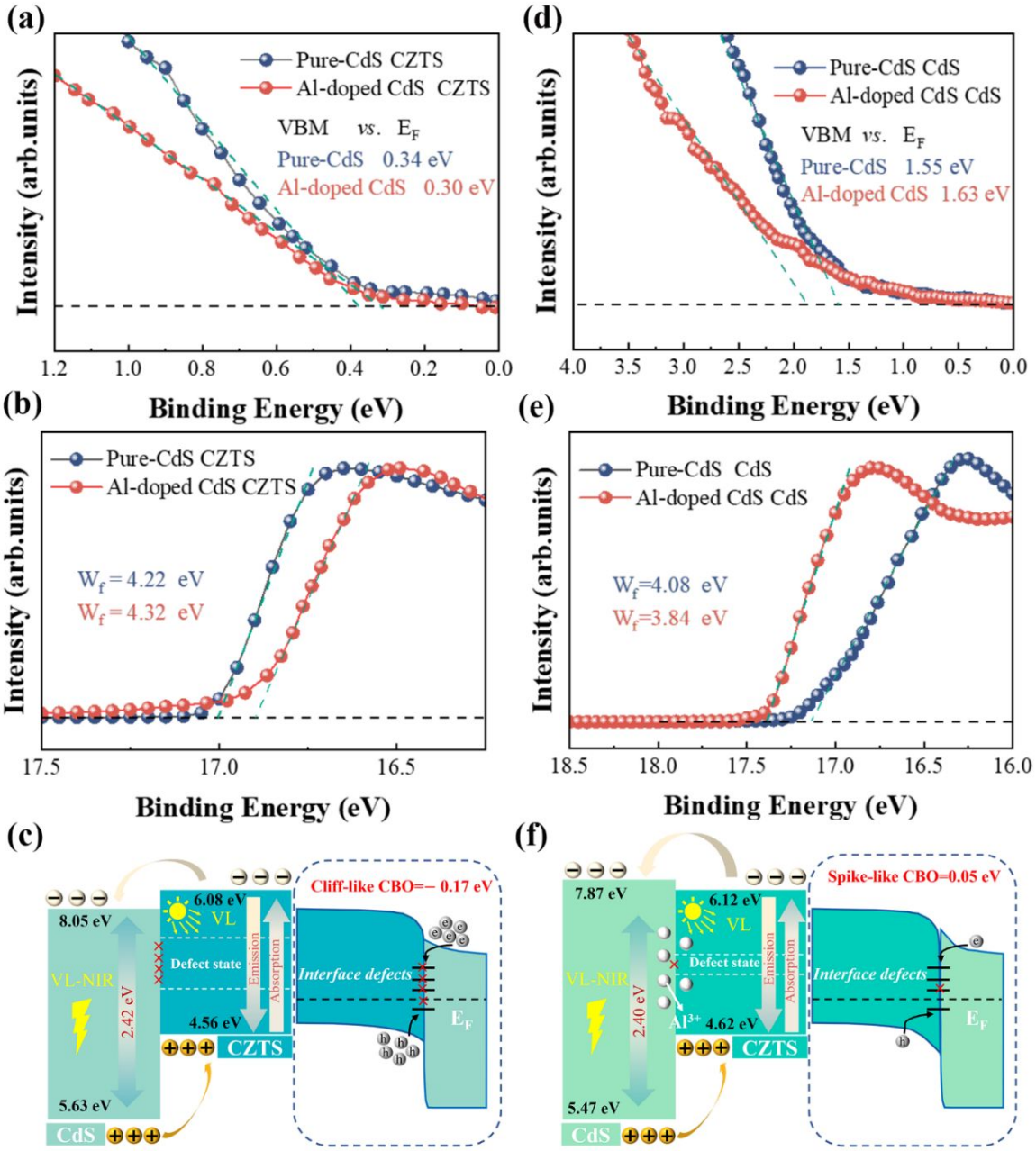

Figure 3. (a), (b), (d) and (e) are the UPS spectra of pure-CdS and Al-doped CdS devices.

Schematic illustration of the band alignment for pure-CdS (c) and Al-doped CdS (f) devices.

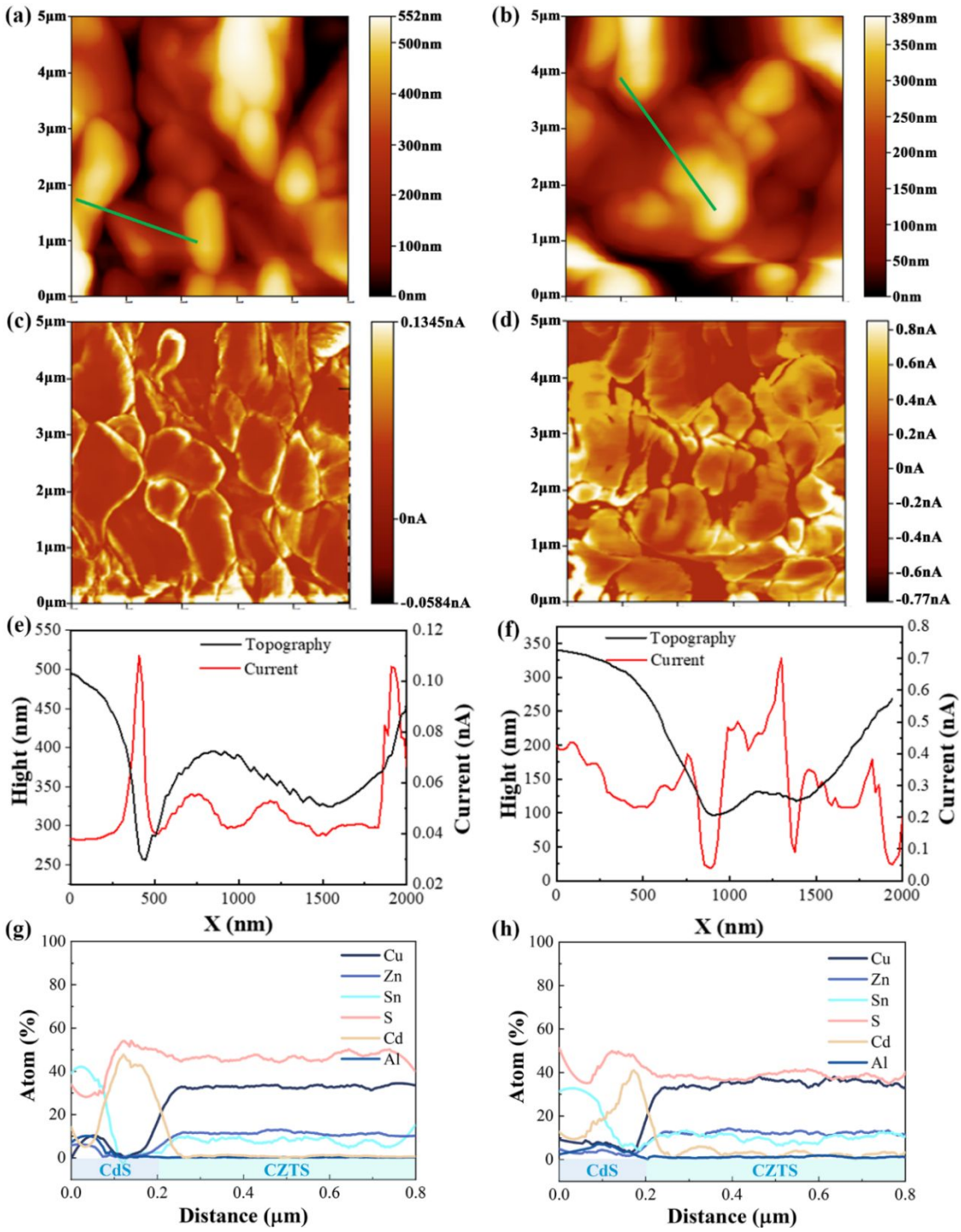

Figure 4. Surface morphology of the pure-CdS (a) and Al-doped CdS (b) devices. (c) C-AFM image and the corresponding potential curve (e) at the scribe line of the pure-CdS device. (d) C-AFM image and the corresponding potential curve (f) at the scribe line of the Al-doped CdS devices. EDS elemental line scan profiles across the CZTS/CdS of the pure-CdS (g) and Al-doped CdS (h) devices.

In the heat treatment process, the doped and other elements have a thermodynamic process between the heterojunctions. Transmission Electron Microscope-Energy Dispersive Spectroscopy (TEM-EDX) and high-angle-annular-dark-field (HAADF) were used to deeply examine the interdiffusion of elements at CdS/CZTS (**Figure 4 and S6**). The EDS line scan and composition distribution diagrams show that, the heterojunction annealing promotes the inter-element diffusion between the CdS/CZTS interface and is mainly manifested in the slight increase of copper, zinc, and tin in the CdS layer at the heterojunction region; and the existence of Cd is also found in the CZTS. Only a small amount of Al (~1%) exists in the CZTS absorber, but ~10% of Al is detected in CdS. Therefore, the diffusion of Al in CdS is much larger than that in the CZTS absorber. The finding shows the diffusion within the heterojunction, and its effect on the heterojunction at the buffer layer was more than that at the interface of the heterojunction. In addition, the surface scan distribution of the device cross-section shows the uniform distribution of each element in the absorber layer, showing the excellent compactness and uniformity of the absorber layer.

Figures 5 (a) –(d) shows the statistical distribution of device parameters (V_{OC}, J_{SC}, FF, and PCE) with different Al doping concentrations. Sixteen devices were fabricated on each type of absorber layer film, and the variation in performance between individual devices further demonstrated the cracking uniformity of the films and the repeatability of the device fabrication process. The changing trend of each parameter in the figure that with the increase shows in doping concentration, the main parameters of the device have slow progress with increasing doping concentration. When the doping concentration of Al reaches 0.3%, the performance of the device begins to deteriorate. A more suitable heterojunction doping concentration of 0.2% was obtained. Diode parameters were studied systematically to further examine the influence

of doping concentration on the recombination mechanism. The parallel conductance G, series resistance R, diode ideality factor A and reverse saturation current density J_0 of the device are obtained according to the general single exponential equation of the diode, and the formula[40] is as follows:

$$J = J_0 exp\left[\frac{q}{AkT}(V - RJ)\right] + GV - J_L \quad (1)$$

where J_L is the short-circuit current in the light state. The device displayed the diode rectification features shown in **Figure 5(f)**. When voltage is applied in the dark, representing the general characteristics of high-efficiency solar cells. The relationship between dJ/dV and voltage V is as shown in **Figure 5(g)**. The parallel conductance of devices with different doping concentrations is obtained by calculation. The G value reached 0.52, 0.61, 0.27, and 0.7 mS cm^{-2} with the increase in doping concentration. Series resistance R and diode ideality factor A are obtained by plotting $dV/dJ \sim (J + J_{SC})^{-1}$ and extrapolating the curve to the Y-axis and that calculated from the slope AkT/q, respectively. The calculation results are shown in the figure, and the date analysis indicates that the doping with 0.2% Al ion concentration has the smallest series resistance and ideality factor, resulting in less recombination at the heterojunction interface. A higher ideal factor A indicates a more severe Shockley–Hall recombination in the depletion region of the device, which may arise from high defect concentrations near the absorber surface.[41] In addition, the decrease in the series resistance R may contribute to the increased in FF. The reverse saturation current density J_0 is calculated from the curve $\ln(J + J_{SC}\text{-}GV) \sim V\text{-}RJ$, as shown in **Figure 5(i)**. The directional saturation currents are 5.5×10^{-7}, 3.9×10^{-7}, 2.2×10^{-7}, and 5.6×10^{-6} mA cm^{-2} with the increase in doping concentration, the lowest value is obtained when the doping concentration is 0.2%. A smaller reverse saturation current is usually evidence of better unidirectional conductivity of the diode. Therefore, the appropriate

doping concentration can greatly improve the quality of the solar cell CZTS/CdS heterojunction, and the series resistance and reverse saturation current decrease with the introduction of dopants, greatly improving the device performance.

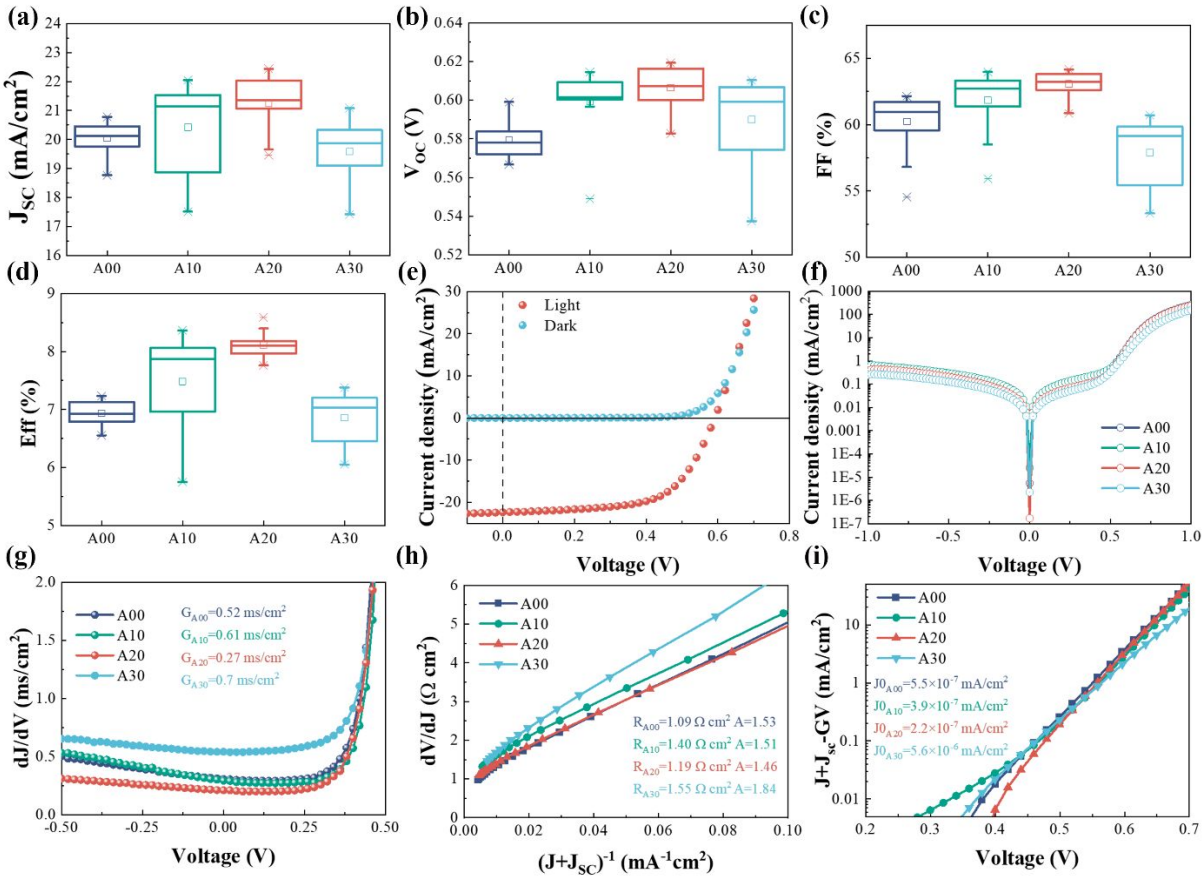

Figure 5. (a)-(d) Statistical chart of predominant performance parameters of solar cells with different doping concentration. Electrical behaviors of the devices (A00, A10, A20, and A30): (e) Dark *J-V* curves, (f) Rectifier characteristic curves of solar cells with different Al doping concentrations, (g) Shunt conductance G characterization, (h) Series resistance R and ideality factor A characterization, (i) Reverse saturation current density J_0 characterization.

To obtain detailed information about carrier concentration, deep-level defects and heterojunction interface states, capacitance–voltage (C-V) and drive-level capacitance profiling (DLCP) tests were performed for CZTS devices with different concentrations. Generally, the signals of C-V and DLCP tests include deep-level information on defect and carrier

concentration. In addition, the concentration difference between C-V and DLCP curves at 0 V bias reflects the interface state information of the heterojunction.[42-44] Equation 2 represents the CV and the DLCP relationship for Nc-v and N_{DLCP} plots.

$$\begin{cases} N_{C-V} = \frac{C^3}{qA^2\varepsilon_0\varepsilon_s}\left(\frac{dC}{dV}\right)^{-1}, \\ N_{DLCP} = -\frac{C_0^3}{2q\varepsilon_0\varepsilon_s A^2 C_1}, \\ x = \varepsilon_0\varepsilon_S A/C \end{cases} \quad (2)$$

where A = active area, ε_0= dielectric constant for vacuum (≈8.854×10^{-12} Fm^{-1}), ε_s = relative dielectric constant for CZTS (≈8), C is the measure capacitance (5.2×10^{-9}~1×10^{-8} F), and C_0 is the minimum limiting value of capacitance as AC.[45,46] As illustrated in **Figure 6**, the width of the depletion region of the device decreases from 164 nm to 95 nm as the doping proceeds. The width of the depletion layer is an important parameter for thin-film solar cells, especially for materials with short carrier diffusion lengths such as CZTS and CIGS, etc. The transport of photogenerated carriers in thin-film solar cells mainly depends on the built-in electric field. High-efficiency devices usually require a higher depletion layer width. In this experiment, although the depletion layer width decreases with the doping, the more important parameter affecting the performance of the device is the size of the defect concentration. **Table 3** records the specific values of each performance parameter of the device. Compared with the undoped CZTS device, the interface state density (N_{CV}-N_{DL}) decreased from 4.7×10^{15} cm^{-3} to 1.2×10^{15} cm^{-3}. In addition, the N_{CV} and N_{DL} of the device decreased significantly with the addition of dopants. The N_{CV} of the 0.2% Al-doped device decreased from 5.25×10^{16} cm^{-3} undoped to 3.75×10^{16} cm^{-3} doped, and the N_{DL} was reduced from 4.78×10^{16} cm^{-3} to 3.63×10^{16} cm^{-3} after doping. **Figure 6(b)** shows the EIS test to demonstrate the charge recombination and transportation in CZTS solar cells. As a characterization of minority carrier recombination

characteristics, EIS has been widely used in the research of some photovoltaic devices, corresponding to the EIS images of CZTS solar cells doped with different concentrations of Al ions. The fitting curve of the solid line is obtained by fitting the original data, and the corresponding fitting parameters are presented in **Table 3**. The intercept between the starting point of the curve and the X-axis shown in **Figure 6(b)** represents the series resistance. As the doping concentration increases, the series resistance of the device is 17.62, 16.49, 12.45, and 19.36 Ω. In addition, the diameter of the semi-circle represents the composite resistance of the device. As the doping concentration increases, the composite resistance of the device is 25225, 35117, 68471, and 36006 Ω, thereby obtaining the device at a doping concentration of 0.2%. It has the smallest series resistance and the largest composite resistance, which represents the excellent optoelectronic performance of the device, it is also consistent with the previous test and characterization analysis. The reduction of series resistance may be the main reason for the superior J_{SC} of our device.

Table 3. Summary of results derived from C–V and DLCP measurements and EIS.

Device	N_{CV} (cm $^{-3}$)	N_{DLCP} (cm $^{-3}$)	Interface state response (relative values)	Depletion width (nm)	R_S (Ω)	R_{rec} (Ω)
A00	5.25×10^{16}	4.78×10^{16}	4.7×10^{15}	164.94	17.62	25225
A10	4.24×10^{16}	4.22×10^{16}	2.0×10^{14}	156.23	16.49	35117
A20	3.75×10^{16}	3.63×10^{16}	1.2×10^{15}	139.09	12.45	68471

A30	6.75×10^{16}	6.37×10^{16}	3.8×10^{15}	95.10	19.36	36006

TRPL was used to investigate the minority carrier's lifetime with or without Al-doped, and the result of the device is shown in **Figure 6(c)**, illustrating the minority carrier lifetime decay curves of devices with a concentration of 0.2%. The figure shows that with the doping of Al ions, the minority carrier lifetime of the device improves surprisingly from 3.09 ns to 4.6 ns. **Figure S7** shows the influence of Al doping concentration on minority carrier lifetime and it reaches to 4.6 ns at 0.2%. When the concentration increases to 0.3%, the lifetime decreases to 2.01 ns. This result shows that the nonradiative recombination due to deep-level defects is considerably decreased with a suitable Al-doping concentration. Deep-level transient spectroscopy (DLTS) was used to explore the dynamics of defect properties to obtain more information about deep-level defects. **Figure 5(d)** exhibits the DLTS signals comprising positive (majority carrier traps) and negative peaks (minority carrier traps).[47] An electron trap E1 can be recognized in an Al-doped device, and remarkably, a new hole trap H1 appears in the untreated device. Evidently, the Ea values of 0.25–0.42 eV correspond to CuSn antistites acceptors defects.[48,49] The disappearance of this additional hole trap may be attributed to the reduction of Cu_{Sn} antistites by doping annealing, thereby promoting Cd diffusion. These defects are known to be deep-level defects, which are unfavorable to the efficiency of solar cell devices. The defect characteristics such as activation energy (E_r), defect density (N_T), capture cross-section (σ), and $N_T \times \sigma$, are presented in **Table 4**. Especially, the E_r (E_C–E_T or E_T–E_V, wherein, E_T, E_C, and E_V are the defect energy level, conduction band edge, and valance band edge, respectively) of the defects were obtained through the linear fitting of DLTS signal derived Arrhenius plot points (**Figure 6 (e)**), using the following equations: [50]

$$\ln\left(\tau_e \upsilon_{th,n} N_C\right) = \frac{E_C - E_T}{k_B T} - \ln\left(X_n \sigma_n\right) \quad (3)$$

$$\ln\left(\tau_e \upsilon_{th,p} N_V\right) = \frac{E_T - E_V}{k_B T} - \ln\left(X_p \sigma_p\right) \quad (4)$$

where τ_e is the emission time constant, $\upsilon_{th,n}$ and $\upsilon_{th,p}$ are the thermal velocity, N_C, N_V represent conduction band state density and valence band state density, respectively. X_n and X_p are the entropy factor for electron and hole. The corresponding energy level of the negative peak for the Al-doped device was detected at 0.223 eV with a N_T and σ of 3.62×10^{12} cm^{-3} and 9.86×10^{-21} cm^2, respectively. The pure-CdS device exhibited a defect type E1 located at about 0.331 eV, a longing with an adversely increased N_T of 2.48×10^{14} cm^{-3}, and a largest σ of 1.39×10^{-20} cm^2. Speciously, the defect E1 value for the Al-doped device is lower than that of the control device, but the density of Cu_{Sn} defects decreased from 2.48×10^{14} to 3.62×10^{12} cm^{-3} with Al-doping. Notably, the decreased defect density and capture cross-section of the CZTS device with the doping of Al cation improved the performance. Furthermore, the index $N_T\times\sigma$ is another effective pathway to investigate the defect feature for thin film solar cells, calculating from the following equation:[51]

$$\tau_{trap} = \frac{1}{v_t \sigma N_T} \quad (5)$$

where σ and N_T are the capture cross-section and defect density acquired from DLTS results, υ_t is the carrier thermal velocity, approximate to 10^7 cm s^{-1} at a room temperature in the bulk of semiconductors.

Table 4. Defect characteristics of the two devices.

Device	Defects	E_r (eV)	N_T (cm^{-3})	σ (cm^2)	$N_T\times\sigma$ (cm^{-1})
Al-doped CdS	E1	0.223	3.62×10^{12}	9.86×10^{-21}	3.57×10^{-8}
Pure-CdS	E1	0.331	2.48×10^{14}	1.39×10^{-20}	3.45×10^{-6}

H1	0.290	9.16×10^{12}	1.25×10^{-18}	1.15×10^{-5}

As shown in **Table 4**, the obviously decreased $N_T \times \sigma$ value revealed an efficiency passivation of the major defects (E1), owing to the Al doping in the CZTS after heat annealing. Evidently, the photogenerated electrons and holes are likely to be captured leading to awful trap-assisted recombination, ultimately reducing the minority carrier lifetime, which could decrease the value of J_{SC}. And carriers trapped by the shallow trap will be emitted again in a very short time due to the reduction of the capture cross-section. **Figure 6(f)** show the energy states and defect levels of the two devices. The defect level E1 of Al-doped extracted from the Arrhenius plots was located at 0.223 eV below E_C, and the defect level E1 of pure-CdS was located at 0.331 eV below E_C, which were closer to the position of its intrinsic E_F, it will lead to severe defect-assisted recombination because of the detrimental pining effect. In this work, the situation is improved by Al ion doping with heat treatment.

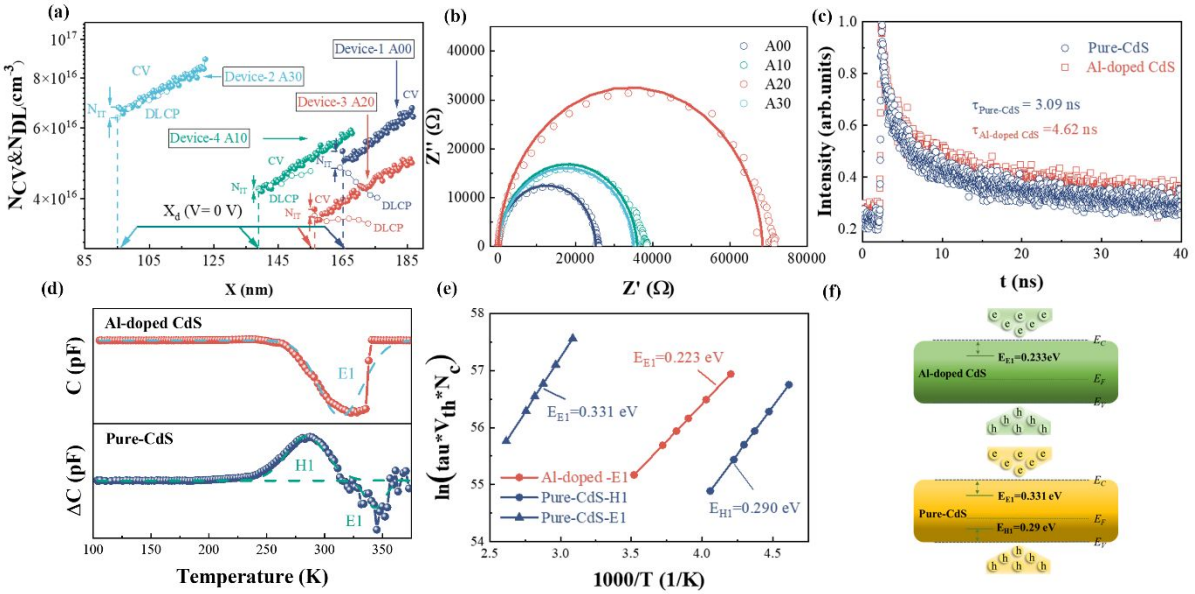

Figure 6. (a) The CV and DLCP profiles. (b) Nyquist plots of the impedance for A00, A10, A20 and A30 device. (c) Time-resolved photoluminescence decay at 532 nm excitation for

pure-CdS and Al-doped devices. (d) DLTS spectra (e) Arrhenius plots obtained from DLTS. (f) Schematic diagram of defects in pure-CdS and Al-doped CdS devices.

4. Conclusion

Herein, a two-step heterojunction heat treatment combined with Al doping strategy was developed to enhance the interfacial performance of CZTS solar cells. A champion PCE of 8.65% was attained, the highest value of which for CZTS prepared by PLD thus far. Further investigation revealed that the two-step annealing optimizes the quality of heterojunction and promotes the passivation of interface defects. During the process of two-step annealing, a simple spin-coating was used to realize the diffusion of Al^{3+} at the CdS/CZTS heterojunction interface. The P-type and N-type carrier concentrations were significantly increased by substitution doping of Cd and Sn. In addition, the doping of Al^{3+} reduces the conduction band offset of the heterojunction to achieve a more favorable band alignment, which effectively inhibited the nonradiative recombination of interface carriers. More importantly, the tested minority carrier lifetime of the device improved to 4.6 ns, which resulted in higher current harvesting efficiency. Thus, the CZTS solar cell presents lower interfacial defect density, slower recombination rate, and higher charge collection efficiency. The fill factor and J_{SC} of the final PLD-based CZTS device are increased to 64.06% and 22.33 mA cm^{-2}, respectively, even exceeding the relevant parameters of the current CZTS solar cell with the highest PCE. It provides an experimental reference for further improving the conversion efficiency of CZTS thin film solar cells.

Supporting information

Additional SEM images, XRD, film morphology, EDS and Electrical behaviors of the samples.

Acknowledgements

This work was supported by National Natural Science Foundation of China (62074102) China, Guangdong Basic and Applied Basic Research Foundation (2022A1515010979) China, Science and Technology plan project of Shenzhen (20200826143347001 and 20220808165025003) China.

Conflicts of Interest

There are no conflicts to declare.

Data Availability Statement

The original data in this work is available from the corresponding authors upon reasonable request.

References

(1) Yan, C.; Huang, J.; Sun, K.; Johnston, S.; Zhang, Y.; Sun, H.; Pu, A.; He, M.; Liu, F.; Eder, K.; Yang, L.; Cairney, J. M.; Ekins-Daukes, N. J.; Hameiri, Z.; Stride, J. A.; Chen, S.; Green, M. A.; Hao, X. Cu_2ZnSnS_4 solar cells with over 10% power conversion efficiency enabled by heterojunction heat treatment. *Nat. Energy* **2018,** *3*, 764-772.

(2) Green, M. A.; Dunlop, E. D.; Hohl-Ebinger, J.; Yoshita, M.; Kopidakis, N.; Bothe, K.; Hinken, D.; Rauer, M.; Hao, X. Solar cell efficiency tables (Version 60). *Prog. Photovoltaics Res. Appl.* **2022,** *30*, 687-701.

(3) Li, S.-Y.; Hägglund, C.; Ren, Y.; Scragg, J. J. S.; Larsen, J. K.; Frisk, C.; Rudisch, K.; Englund, S.; Platzer-Björkman, C. Optical properties of reactively sputtered Cu_2ZnSnS_4 solar absorbers determined by spectroscopic ellipsometry and spectrophotometry. *Sol. Energy Mater. Sol. Cells* **2016,** *149*, 170-178.

(4) Sarswat, P. K.; Free, M. L. A study of energy band gap versus temperature for Cu_2ZnSnS_4 thin films. *Physica B* **2012,** *407*, 108-111.

(5) Sánchez, T. G.; Mathew, X.; Mathews, N. R. Obtaining phase-pure CZTS thin films by annealing vacuum evaporated CuS/SnS/ZnS stack. *J. Cryst. Growth* **2016,** *445*, 15-23.

(6) Shin, D.; Saparov, B.; Mitzi, D. B. Defect Engineering in Multinary Earth - Abundant Chalcogenide

Photovoltaic Materials. *Adv. Energy Mater.* **2017,** *7*, 1602366.

(7) He, W.; Sui, Y.; Zeng, F.; Wang, Z.; Wang, F.; Yao, B.; Yang, L. Enhancing the Performance of Aqueous Solution-Processed Cu(2)ZnSn(S,Se)(4) Photovoltaic Materials by Mn(2+) Substitution. *Nanomaterials (Basel, Switzerland)* **2020,** *10*, 1250.

(8) Cui, Y.; Zhao, K.; Liu, C.; Xiang, H.; Liang, H.; Jia, Y. Band Edge Engineering for the Improvement of Open-Circuit Voltage: Ag-Based Selenized Cu2ZnSn(SSe)4 Surface Regulated by Lithium. *Solar RRL* **2021,** *5*, 2000631.

(9) He, M.; Sun, K.; Suryawanshi, M. P.; Li, J.; Hao, X. Interface engineering of p-n heterojunction for kesterite photovoltaics: A progress review. *J. Energy Chem.* **2021,** *60*, 1-8.

(10) He, M.; Yan, C.; Li, J.; Suryawanshi, M. P.; Kim, J.; Green, M. A.; Hao, X. Kesterite Solar Cells: Insights into Current Strategies and Challenges. *Adv. Sci. (Weinh)* **2021,** *8*, 2004313.

(11) Nisika; Kaur, K.; Kumar, M. Progress and prospects of CZTSSe/CdS interface engineering to combat high open-circuit voltage deficit of kesterite photovoltaics: a critical review. *J. Mater. Chem. A* **2020,** *8*, 21547-21584.

(12) Gang, M. G.; Karade, V. C.; Suryawanshi, M. P.; Yoo, H.; He, M.; Hao, X.; Lee, I. J.; Lee, B. H.; Shin, S. W.; Kim, J. H. A Facile Process for Partial Ag Substitution in Kesterite $Cu_2ZnSn(S,Se)_4$ Solar Cells Enabling a Device Efficiency of over 12. *ACS Appl. Mater. Interfaces* **2021**, *13*, 3959-3968.

(13) Hadke, S. H.; Levcenko, S.; Lie, S.; Hages, C. J.; Márquez, J. A.; Unold, T.; Wong, L. H. Synergistic Effects of Double Cation Substitution in Solution-Processed CZTS Solar Cells with over 10% Efficiency. *Adv. Energy Mater.* **2018,** *8*, 1802540.

(14) Ibrahim, A.; Guchhait, A.; Hadke, S.; Seng, H. L.; Wong, L. H. Silver and Potassium Incorporation in Double-Layer Solution-Processed Cu2ZnSnS4 Solar Cell. *ACS Appl. Energy Mater.* **2020,** *3*, 10402-10407.

(15) Fan, P.; He, Y.; Liang, G.; Xie, Z.; Yu, Z.; Lin, J.; Chen, S.; Zheng, Z.; Luo, J.; Su, Z. Enhancing Ag-alloyed Cu_2ZnSnS_4 solar cell performance by interfacial modification via In and Al. *J. Mater. Chem. A* **2021,** *9*, 25196-25207.

(16) Gansukh, M.; López Mariño, S.; Espindola Rodriguez, M.; Engberg, S. L. J.; Martinho, F. M. A.; Hajijafarassar, A.; Schjødt, N. C.; Stamate, E.; Hansen, O.; Schou, J.; Canulescu, S. Oxide route for production of Cu_2ZnSnS_4 solar cells by pulsed laser deposition. *Sol. Energy Mater. Sol. Cells* **2020,** *215*, 110605.

(17) Dimitrievska, M.; Fairbrother, A.; Fontané, X.; Jawhari, T.; Izquierdo-Roca, V.; Saucedo, E.; Pérez-Rodríguez, A. Multiwavelength excitation Raman scattering study of polycrystalline kesterite Cu_2ZnSnS_4 thin films. *Appl. Phys. Lett.* **2014,** *104*, 021901.

(18) Scragg, J. J. S.; Choubrac, L.; Lafond, A.; Ericson, T.; Platzer-Björkman, C. A low-temperature order-disorder transition in Cu_2ZnSnS_4 thin films. *Appl. Phys. Lett.* **2014,** *104*, 041911.

(19) Valentini, M.; Malerba, C.; Menchini, F.; Tedeschi, D.; Polimeni, A.; Capizzi, M.; Mittiga, A. Effect of the order-disorder transition on the optical properties of Cu_2ZnSnS_4. *Appl. Phys. Lett.* **2016,** *108*, 211909.

(20) Bourdais, S.; Choné, C.; Delatouche, B.; Jacob, A.; Larramona, G.; Moisan, C.; Lafond, A.; Donatini, F.; Rey, G.; Siebentritt, S.; Walsh, A.; Dennler, G. Is the Cu/Zn Disorder the Main Culprit for the Voltage Deficit in Kesterite Solar Cells? *Adv. Energy Mater.* **2016,** *6*, 1502276.

(21) Kermadi, S.; Sali, S.; Ait Ameur, F.; Zougar, L.; Boumaour, M.; Toumiat, A.; Melnik, N. N.; Hewak, D. W.; Duta, A. Effect of copper content and sulfurization process on optical, structural and electrical properties of ultrasonic spray pyrolysed Cu_2ZnSnS_4 thin films. *Mater. Chem. Phys.* **2016,** *169*, 96-104.

(22) Ge, J.; Wu, Y.; Zhang, C.; Zuo, S.; Jiang, J.; Ma, J.; Yang, P.; Chu, J. Comparative study of the influence of two distinct sulfurization ramping rates on the properties of Cu_2ZnSnS_4 thin films. *Appl. Surf. Sci.* **2012,** *258*, 7250-7254.

(23) Moriya, K.; Tanaka, K.; Uchiki, H. Fabrication of Cu_2ZnSnS_4 Thin-Film Solar Cell Prepared by Pulsed Laser Deposition. *Jpn. J. Appl. Phys.* **2007,** *46*, 5780-5781.

(24) Moriya, K.; Tanaka, K.; Uchiki, H. Cu_2ZnSnS_4 Thin Films Annealed in H_2S Atmosphere for Solar Cell Absorber Prepared by Pulsed Laser Deposition. *Jpn. J. Appl. Phys.* **2008,** *47*, 602-604.

(25) Jin, X.; Yuan, C.; Jiang, G.; Liu, W.; Zhu, C. Pulsed laser deposition of Cu_2ZnSnS_4 thin films from single quaternary sulfide target prepared by combustion method. *Mater. Lett.* **2016,** *175*, 180-183.

(26) Cazzaniga, A.; Crovetto, A.; Yan, C.; Sun, K.; Hao, X.; Ramis Estelrich, J.; Canulescu, S.; Stamate, E.; Pryds, N.; Hansen, O.; Schou, J. Ultra-thin Cu_2ZnSnS_4 solar cell by pulsed laser deposition. *Sol. Energy Mater. Sol. Cells* **2017,** *166*, 91-99.

(27) Hu, J.-G.; Wu, T.; Ishaq, M.; Farooq, U.; Chen, S.; Zheng, Z.-H.; Su, Z.-H.; Lin, X.-D.; Fan, P.; Ma, H.-L.; Zhang, X.-H.; Liang, G.-X. Pulsed laser deposited and sulfurized Cu_2ZnSnS_4 thin film for efficient solar cell. *Sol. Energy Mater. Sol. Cells* **2021,** *233*, 111383.

(28) Liang, G.-X.; Luo, Y.-D.; Chen, S.; Tang, R.; Zheng, Z.-H.; Li, X.-J.; Liu, X.-S.; Liu, Y.-K.; Li, Y.-F.; Chen, X.-Y.; Su, Z.-H.; Zhang, X.-H.; Ma, H.-L.; Fan, P. Sputtered and selenized Sb_2Se_3 thin-film solar cells with open-circuit voltage exceeding 500 mV. *Nano Energy* **2020,** *73*, 104806.

(29) Hages, C. J.; Koeper, M. J.; Agrawal, R. Optoelectronic and material properties of nanocrystal-based CZTSe absorbers with Ag-alloying. *Sol. Energy Mater. Sol. Cells* **2016,** *145*, 342-348.

(30) Hadke, S.; Levcenko, S.; Sai Gautam, G.; Hages, C. J.; Márquez, J. A.; Izquierdo-Roca, V.; Carter, E. A.; Unold, T.; Wong, L. H. Suppressed Deep Traps and Bandgap Fluctuations in Cu_2CdSnS_4 Solar Cells with ≈8% Efficiency. *Adv. Energy Mater.* **2019,** *9*, 1902509.

(31) Gershon, T.; Lee, Y. S.; Antunez, P.; Mankad, R.; Singh, S.; Bishop, D.; Gunawan, O.; Hopstaken, M.; Haight, R. Photovoltaic Materials and Devices Based on the Alloyed Kesterite Absorber $(AgxCu1\text{-}x)_2ZnSnSe_4$. *Adv. Energy Mater.* **2016,** *6*, 1502468.

(32) Karade, V. C.; Suryawanshi, M. P.; Jang, J. S.; Gour, K. S.; Jang, S.; Park, J.; Kim, J. H.; Shin, S. W. Understanding defects and band tailing characteristics and their impact on the device performance of $Cu_2ZnSn(S,Se)_4$ solar cells. *J. Mater. Chem. A* **2022,** *10*, 8466-8478.

(33) Fan, P.; Lin, J.; Hu, J.; Yu, Z.; Zhao, Y.; Chen, S.; Zheng, Z.; Luo, J.; Liang, G.; Su, Z. Over 10% Efficient Cu_2CdSnS_4 Solar Cells Fabricated from Optimized Sulfurization. *Adv. Funct. Mater.* **2022,** *32*, 2207470.

(34) Sun, K.; Yan, C.; Liu, F.; Huang, J.; Zhou, F.; Stride, J. A.; Green, M.; Hao, X. Over 9% Efficient Kesterite Cu_2ZnSnS_4 Solar Cell Fabricated by Using $Zn_{1-x}Cd_xS$ Buffer Layer. *Adv. Funct. Mater.* **2016,** *6*, 1600046.

(35) Crovetto, A.; Hansen, O. What is the band alignment of $Cu_2ZnSn(S,Se)_4$ solar cells? *Sol. Energy Mater. Sol. Cells* **2017,** *169*, 177-194.

(36) Turnbull, M. J.; Yiu, Y. M.; Goldman, M.; Sham, T. K.; Ding, Z. Favorable Bonding and Band Structures of Cu(2)ZnSnS(4) and CdS Films and Their Photovoltaic Interfaces. *ACS Appl. Mater. Interfaces* **2022**, *14*, 32683-32695.

(37) Yan, C.; Liu, F.; Song, N.; Ng, B. K.; Stride, J. A.; Tadich, A.; Hao, X. Band alignments of different buffer layers (CdS, Zn(O,S), and In_2S_3) on Cu_2ZnSnS_4. *Appl. Phys. Lett.* **2014,** *104*, 173901.

(38) Zhao, Q.; Shen, H.; Xu, Y.; Gao, K.; Chen, D.; Li, Y. Effect of CZTS/CCZTS Stacked Structures Prepared through Split-Cycle on the Performance of Flexible Solar Cells. *ACS Appl. Energy Mater.* **2022,** *5*, 3668–3676.

(39) Duan, B.; Lou, L.; Meng, F.; Zhou, J.; Wang, J.; Shi, J.; Wu, H.; Luo, Y.; Li, D.; Meng, Q. Two-Step Annealing CZTSSe/CdS Heterojunction to Improve Interface Properties of Kesterite Solar Cells. *ACS Appl. Mater. Interfaces* **2021**, *13*, 55243-55253.

(40) Liang, G.; Chen, M.; Ishaq, M.; Li, X.; Tang, R.; Zheng, Z.; Su, Z.; Fan, P.; Zhang, X.; Chen, S. Crystal Growth Promotion and Defects Healing Enable Minimum Open-Circuit Voltage Deficit in Antimony Selenide Solar Cells. *Adv Sci (Weinh)* **2022,** *9*, e2105142.

(41) Gong, Y.; Zhang, Y.; Zhu, Q.; Zhou, Y.; Qiu, R.; Niu, C.; Yan, W.; Huang, W.; Xin, H. Identifying the origin of the Voc deficit of kesterite solar cells from the two grain growth mechanisms induced by Sn^{2+} and Sn^{4+}

precursors in DMSO solution. *Energy Environ. Sci.* **2021,** *14*, 2369-2380.

(42) Fan, P.; Xie, Z.; Liang, G.; Ishaq, M.; Chen, S.; Zheng, Z.; Yan, C.; Huang, J.; Hao, X.; Zhang, Y.; Su, Z. High-efficiency ultra-thin Cu_2ZnSnS_4 solar cells by double-pressure sputtering with spark plasma sintered quaternary target. *J. Energy Chem.* **2021,** *61*, 186-194.

(43) Todorov, T.; Hillhouse, H. W.; Aazou, S.; Sekkat, Z.; Vigil-Galán, O.; Deshmukh, S. D.; Agrawal, R.; Bourdais, S.; Valdés, M.; Arnou, P.; Mitzi, D. B.; Dale, P. J. Solution-based synthesis of kesterite thin film semiconductors. *J. Phys.: Energy* **2020,** *2*, 012003.

(44) Li, J.; Huang, Y.; Huang, J.; Liang, G.; Zhang, Y.; Rey, G.; Guo, F.; Su, Z.; Zhu, H.; Cai, L.; Sun, K.; Sun, Y.; Liu, F.; Chen, S.; Hao, X.; Mai, Y.; Green, M. A. Defect Control for 12.5% Efficiency $Cu_2ZnSnSe_4$ Kesterite Thin-Film Solar Cells by Engineering of Local Chemical Environment. *Adv Mater* **2020,** *32*, e2005268.

(45) Du, Y.; Wang, S.; Tian, Q.; Zhao, Y.; Chang, X.; Xiao, H.; Deng, Y.; Chen, S.; Wu, S.; Liu, S. Defect Engineering in Earth-Abundant $Cu_2ZnSn(S,Se)_4$ Photovoltaic Materials via Ga^{3+}-Doping for over 12% Efficient Solar Cells. *Adv. Funct. Mater.* **2021,** *31*, 2010325.

(46) Gunawan, O.; Gokmen, T.; Warren, C. W.; Cohen, J. D.; Todorov, T. K.; Barkhouse, D. A. R.; Bag, S.; Tang, J.; Shin, B.; Mitzi, D. B. Electronic properties of the $Cu_2ZnSn(Se,S)_4$ absorber layer in solar cells as revealed by admittance spectroscopy and related methods. *Appl. Phys. Lett.* **2012,** *100*, 253905.

(47) Lian, W.; Jiang, C.; Yin, Y.; Tang, R.; Li, G.; Zhang, L.; Che, B.; Chen, T. Revealing composition and structure dependent deep-level defect in antimony trisulfide photovoltaics. *Nat Commun* **2021,** *12*, 3260.

(48) Gong, Y.; Qiu, R.; Niu, C.; Fu, J.; Jedlicka, E.; Giridharagopal, R.; Zhu, Q.; Zhou, Y.; Yan, W.; Yu, S.; Jiang, J.; Wu, S.; Ginger, D. S.; Huang, W.; Xin, H. Ag Incorporation with Controlled Grain Growth Enables 12.5% Efficient Kesterite Solar Cell with Open Circuit Voltage Reached 64.2% Shockley–Queisser Limit. *Adv. Funct. Mater.* **2021,** *31*, 24.

(49) Fu, J.; Kou, D.; Zhou, W.; Zhou, Z.; Yuan, S.; Qi, Y.; Wu, S. Ag, Ge dual-gradient substitution for low-energy loss and high-efficiency kesterite solar cells. *J. Mater. Chem. A* **2020,** *8*, 22292-22301.

(50) Tang, R.; Wang, X.; Lian, W.; Huang, J.; Wei, Q.; Huang, M.; Yin, Y.; Jiang, C.; Yang, S.; Xing, G.; Chen, S.; Zhu, C.; Hao, X.; Green, M. A.; Chen, T. Hydrothermal deposition of antimony selenosulfide thin films enables solar cells with 10% efficiency. *Nat. Energy* **2020,** *5*, 587-595.

(51) Tang, R.; Chen, S.; Zheng, Z. H.; Su, Z. H.; Luo, J. T.; Fan, P.; Zhang, X. H.; Tang, J.; Liang, G. X. Heterojunction Annealing Enabling Record Open-Circuit Voltage in Antimony Triselenide Solar Cells. *Adv Mater* **2022,** *34*, e2109078.

Table of contents: